FEDSM2022-87470

A STUDY OF MICROFLUIDIC DEVICE GEOMETRIES ON FLUID INSTABILITIES

Sylvain Le Henaff[1], Taylor Peterson[1], Candice Hovell[3], Jeremy Mares[3], Melanie Coathup[2], Veerle Reumers[3], and Michael Kinzel[1]

[1]*University of Central Florida, Department of Mechanical and Aerospace Engineering, Orlando, Florida*
[2]*University of Central Florida, Department of Internal Medicine, Lake Nona, Florida*
[3]*imec USA, Kissimmee, Florida*

ABSTRACT

This effort is focused on studying fluid instabilities in microfluidic devices using Computational Fluid Dynamics (CFD) analysis to provide preliminary data for suborbital microgravity flight experiments. The experiments will utilize a lens-free imaging (LFI) system to capture and measure fluidic data. Various CFD models were created using Star-CCM+ to determine predicted Saffman-Taylor (viscous fingering patterns) instabilities in microfluidic devices using liquids with opposite viscosities. Lab data shows that channel height and inlet nozzle angles of the devices are dominant in the changing behavior of the instabilities. This study will focus on these parameters to further validate CFD results. It is expected that the device geometries will have a large impact on fluid instabilities in the microfluidic domain.

Keywords: *Computational Fluid Dynamics, fluid instability, lens-free imaging, microfluidics, channel flows*

Nomenclature

α_g	Gas volume fraction
α_l	Liquid volume fraction
$\bar{g}$	Force of gravity, m/s^2
μ	Dynamic Viscosity, $Pa \cdot s$
ρ_g	Gas density, kg/m^3
ρ_l	Liquid density, kg/m^3
ρ_m	Mass density, kg/m^3
σ	Surface tension, N/m
h	Channel height, mm
p	Pressure, Pa
Re	Reynold's Number
t	Time, s
u	Inlet velocity, m/s
u,v,w	Fluid velocity terms
u_{max}	Maximum inlet velocity, m/s

Introduction

In recent years, research interest in spaceflight has grown exponentially. Systems act differently in microgravity compared to in normal gravitational forces on Earth. In fluid systems specifically, the lack of gravity takes away any buoyant forces and surface tension dominates, especially for microfluidic flows, such as capillary flow and biofluids. Fluid transport systems that use large pipe diameters are often heavy and generate bubbles with varying microgravity conditions. A solution for this problem is using microfluidic transport systems that utilize capillary forces, which helps save on weight and simplifies complex systems [1]. Capillary flow experiments were done on the International Space Station (ISS) looking at various flow rates through different channel geometries. It was found that increasing the area of the channel decreased the critical mass flow rate [2], which will be seen experimentally later in this paper.

Another area where microfluidic flows are relevant to microgravity relates to the bone health of astronauts. With NASA's mission to go back to the Moon and later Mars, astronauts are spending extended time in microgravity conditions. Even with mandatory exercise for up to 2 and a half hours most days, bone loss is still a common issue [3]. Under weightless conditions, the muscles operate at a lesser load, and this causes a smaller amount of strain on the bones [4]. Due to the nature of microfluidic flow within the porous media of bone structures, this results in bone loss over short periods in low gravity. This is where the dominating surface tension term plays a large role. Similarly, this effect can be seen during fluid instabilities within the displacement of a high viscosity fluid by a lower viscosity fluid. This phenomenon is referred to as the Saffman-Taylor instability, or viscous fingering [5], which will be talked about in more detail in a later section. Saffman and Taylor originally obtained these experimental results in 1958 [6] and found that the angle between the direction of fluid flow and the outward normal direction of the flow, shown

FIGURE 1.   Channel Geometry and Angle Tested

in Figure 1 and from now on referred to as the inlet angle α, will affect the shape of the viscous finger. The fluids used in this study are corn syrup (high viscosity) and ethanol (low viscosity). These were also chosen because they are immiscible fluids, and can be easily modeled within CFD software.

The goals of this study are to experimentally validate the CFD simulations of the viscous fingering with lab results, and in addition test imec's LFI system technology for use on the ISS [7]. The LFI system utilizes digital holography and can achieve sub-cellular resolution with a wide field of view [8]. These characteristics make it an ideal system for use on the ISS as there is no need for the mechanical aspect of traditional optical equipment. This system was used for some experimental results and will be the main source of data collection on an upcoming sub-orbital flight on Blue Origin's New Shepard.

This paper will first discuss the Saffman-Taylor instability in additional detail and then move to computational and experimental methods of observing the viscous fingering within various microfluidic chips with changing inlet angles and channel heights. CFD software is used to make initial predictions using the volume of fluid (VOF) approach. The microfluidic devices are then fabricated and used to conduct lab experiments to validate the CFD simulations. The results are concisely laid out and analyzed for proper discussion, followed by a conclusion and acknowledgments.

Background: Fluid Instabilities

The viscous fingering pattern, or Saffman-Taylor instability, is an important aspect of fluid displacement processes [9]. When a low viscosity fluid v_1 is injected into a high viscosity fluid v_2, the interface between the two will become unstable since the low viscosity fluid is the driving fluid [6]. This will cause the low viscous fluid to create a finger-like pattern, shown in Figure 2. A study by Zimmerman and Homsy [10] found that 2D simulations carry the same results as 3D. These simulations are done in a closely confined, parallel walled space, or what is known as Hele-Shaw Cell [6]. Considering that the channel height is much smaller than the channel length, it is appropriate to assume a Hele-Shaw cell for the geometry. This simplifies the CFD simulation to a 2D scenario which is discussed in the VOF section below. Therefore, showing that 2D simulations are sufficient enough to determine the fluid behavior. The simulations are

recreated at low Reynolds numbers (Re), which is represented by the ratio of viscous forces to inertial forces that are acting on a fluid. In this study, Re is equal to 0.45 in this case, which means that the viscous forces dominate over inertial forces and the flow is laminar.

In this CFD simulation, a channel length of 7 mm is prefilled with a high viscous liquid and injected with a less viscous fluid. The high viscous fluid (corn syrup) has a viscosity of 2.0 $Pa \cdot s$ and the less viscous fluid (ethanol) has a viscosity of 0.001095 $Pa \cdot s$. The viscosity ratio between the high and low viscous fluid is 0.00055. Ethanol is injected into the inlet at 0.02m/s. The channel inlet and outlet angles are 30, 45, and 60 degrees. The channel design is symmetric on the x- and y-axis.
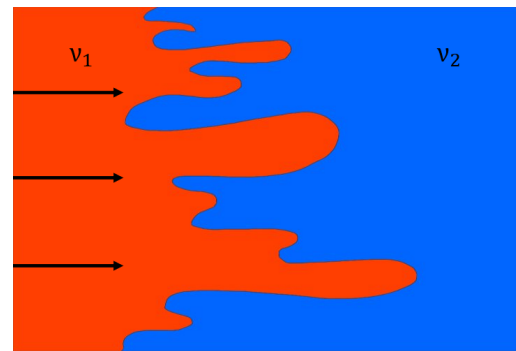
FIGURE 2.   Saffman-Taylor instability: A low viscosity fluid v_1 injected into a high viscosity fluid v_2, creating a viscous fingering pattern.

Methods
Volume of Fluid Method

The CFD software Star-CCM+ utilizes a VOF approach in the simulations with immiscible fluids. VOF is a numerical method for accurately and precisely tracking the location and interaction, like viscous tendencies, between the fluids [11]. The VOF approach goes off of a 'volume-of-fluid function' that will determine the volume fraction in each cell of a given mesh and takes into account a high-resolution interface capturing scheme, surface tension, and contact angles. [12]. This is done by using second-order numerics, such as the conservation of mass, shown in Equation 1 and conservation of momentum equations, shown in Equation 2. Here, the VOF method utilizes the mixture density ρ_m, which is the volume-averaged density of the liquid and gas computed as shown in Equation 3. To obtain the liquid volume fraction α_l, the conservation equation for liquid is utilized as shown in Equation 4. An underlying conservation property applies to volume which implies that the liquid volume fraction plus the gas volume fraction shall equal 1, shown in Equation 5, which enables closure of Equation 3. This system of equations provides a reasonable numerical model for the flows of interest.

$$\frac{\partial \rho_m}{\partial t} + \frac{\partial \rho_m u}{\partial x} + \frac{\partial \rho_m v}{\partial y} + \frac{\partial \rho_m w}{\partial z} = 0 \qquad (1)$$

$$u\frac{\partial (\rho_m u)}{\partial x} = -\frac{\partial p}{dx} + \mu \left(\frac{\partial^2 u}{\partial y^2}\right) + \sigma \frac{\partial^2 \alpha_l}{\partial y^2} + \rho_m \bar{g} \qquad (2)$$

$$\rho_m = \alpha_l \rho_l + \alpha_g \rho_g. \qquad (3)$$

$$\frac{\partial \alpha_l}{\partial t} + \frac{\partial \alpha_l u}{\partial x} + \frac{\partial \alpha_l v}{\partial y} + \frac{\partial \alpha_l w}{\partial z} = 0. \qquad (4)$$
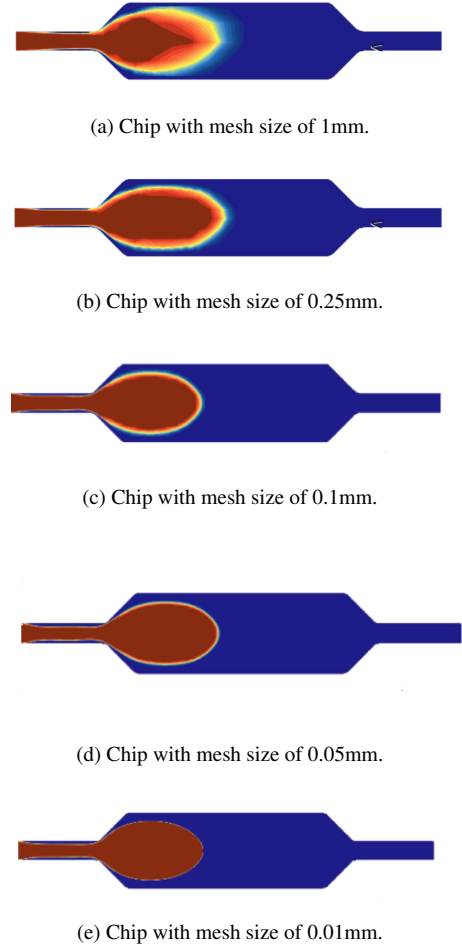
$$\alpha_g + \alpha_l = 1, \qquad (5)$$

The software uses a High Resolution Interface Capturing (HRIC) scheme to solve these equations [13]. Since the flow is at Re < 1, no turbulence model is needed and the solver assumes a laminar flow. HRIC properties include a sharpening factor of 0.0, an angle factor of 0.1, a lower Courant number ($u\frac{\Delta t}{\Delta x}$) of 0.5, and an upper Courant number limit of 2.0. No HRIC gradient smoothing was used.

Other models include surface tension 0.08 as the multiphase interaction, two-dimensional segregated flow, and an adaptive time step of 0.01 seconds. For the contact angle, the Kistler method was used with advancing and receding contact angles of 175 and 20 degrees respectively. The inlet was set as a velocity inlet and the outlet boundary a pressure outlet.

Grid Study

A grid refinement study was performed to ensure that the simulation results accurately reflect the experimental results. Five different mesh sizes were tested and compared using VOF isosurface (contour) measurement of the low viscous fluid as it invades the high viscous fluid.

To begin, a larger mesh size of 1 mm was used which generated a total of 1,012 cells. A second grid size of 0.25 mm was used that contains 1,573 cells. The third, fourth, and fifth grid sizes are 0.1, 0.05, and 0.01 mm and the cell counts are 3,288, 8,792, and 14,869 cells respectively. The VOF results acquired from each simulation with varying mesh sizes can be seen in Figure 3. This figure also shows the difference in the precision of the interface between the two liquids. As can be seen, the smaller the mesh size, the smaller the inter-facial boundary gradient between the two fluids, suggesting a more precise isosurface. Figure 4 shows a plot looking at the isosurface versus different mesh sizes at t=0.6s. The results become increasingly more precise until little change occurs, suggesting mesh convergence. Next, the isosurface values were plotted over time for the different grid sizes, shown in Figure 5. The results are compared

(a) Chip with mesh size of 1mm.

(b) Chip with mesh size of 0.25mm.

(c) Chip with mesh size of 0.1mm.

(d) Chip with mesh size of 0.05mm.

(e) Chip with mesh size of 0.01mm.

FIGURE 3. Simulation results from the same chip, but varying mesh sizes.

and the plots show that 0.05mm and 0.01mm grid sizes converge to give nearly identical results. Due to the high computing time with a 0.01mm size, the 0.05mm grid size is selected to conduct the rest of the study, which can be seen in Figure 6.

Quasi-1D Parametric Model

The next step aims to reduce the model equations to an approximate equation set to study the general trends associated with gravity, velocity, and channel size. This is performed by simplifying the momentum equation into a Quasi 1D, steady-state equation as follows:

$$\rho_m u_{max} \frac{\partial u_{max}}{\partial x} = -\frac{\partial p}{dx} + \mu \frac{u_{max}}{h/2} + \frac{\sigma}{(h/2)^2} + \rho_m \bar{g} \qquad (6)$$

This equation approximates the dependencies for accelerating the fluid in the x-direction. On the right-hand side, the terms
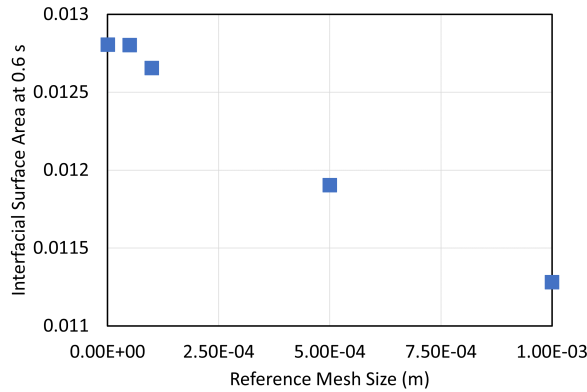
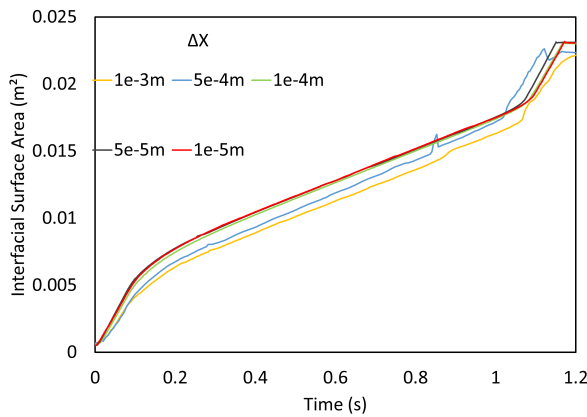**FIGURE 4**. Isosurface at t= 0.6s for Different Mesh Sizes.

FIGURE 5. Isosurface vs Time Plot for Different Mesh Sizes.
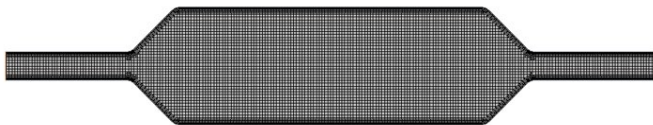

FIGURE 6. Final mesh geometry on the microfluidic chip at 0.05mm.

are sequentially associated with pressure force, viscous force, surface tension force, and finally gravity. These forces can be analyzed as the height of the channel increases, taking a look at the viscous force term in particular. The graph in Figure 7 shows how each force term changes as the channel height of the geometries are increased, with a constant velocity of 0.02m/s. Increasing the channel height will cause the viscous force to decrease exponentially, along with the other forces aside from gravity which stays constant.
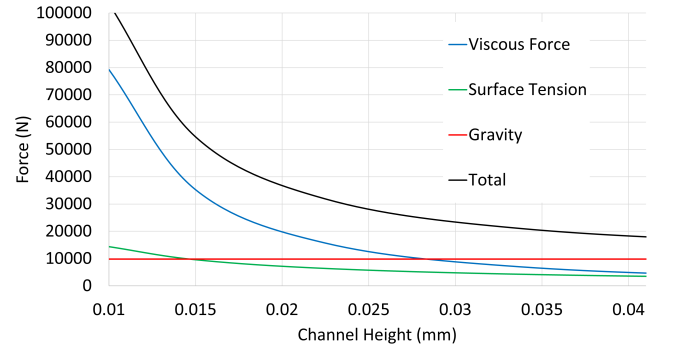

FIGURE 7. Force driving terms graphed against changing channel height of the device with a constant velocity.

Microfluidic Experiments

To benchmark the CFD simulations in Star-CCM+, various experiments were performed in-lab with the 30, 45, and 60 degree inlet angle chips at a height of 700, 200, and 60 micrometers (μm). The microfluidic devices were fabricated using PDMS (Polydimethylsiloxane) that was poured on top of 3D printed molds. The baked PDMS was then plasma-bonded on glass slides for optimal clarity. A syringe pump was used to pump the ethanol into the corn syrup inside the channels at a flow rate of 0.02 m/s which is replicated in the simulation. The clear PDMS allows for the visualization of liquids through microchannels.

Figure 8 shows the experiment results with the ethanol (blue) injected into corn syrup (clear) with a channel height of 700μm. In this experiment, the orientation of gravity points downward on this view of the chip. As the ethanol is injected, it tends to move closer to the top of the channel than the center. This is possible due to the lower density of ethanol compared to corn syrup.

Figure 9 shows the experimental results with the same configurations as before, but the channel height has changed to 200μm.

Figure 10 shows the experimental results with the same set up for a channel height of 60μm. The 30 degree inlet angle is not included in this figure due to difficulties during the experiment, which will be discussed later.

All the experiments were recorded using a Samsung Galaxy S20 camera which does not offer a clear resolution for images at this scale. For better validation and image capture, the experiment will be recorded with higher resolution cameras that can offer better clarity at this scale in the future.

Results and Discussion

Using a mesh size of 0.05mm, mentioned in the Grid Study section, different inlet and outlet angles α in increments of 15 de-
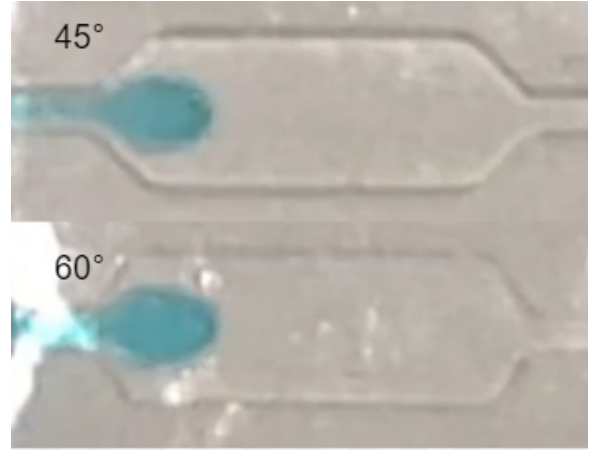
4
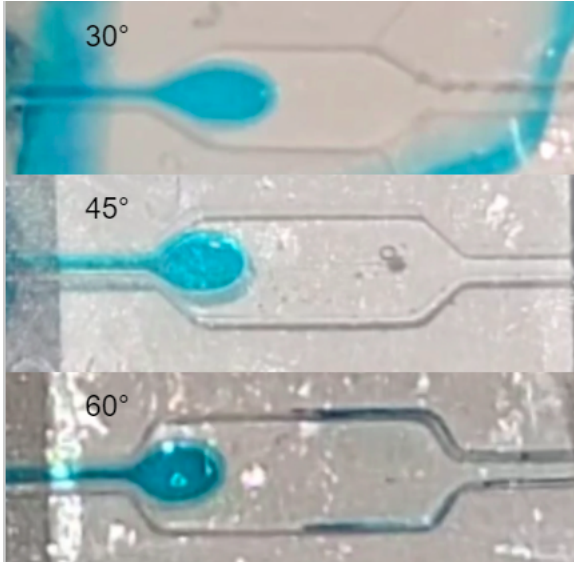
FIGURE 8. Experimental results of a 700μm height chip at 30, 45, and 60 degree inlet angles.
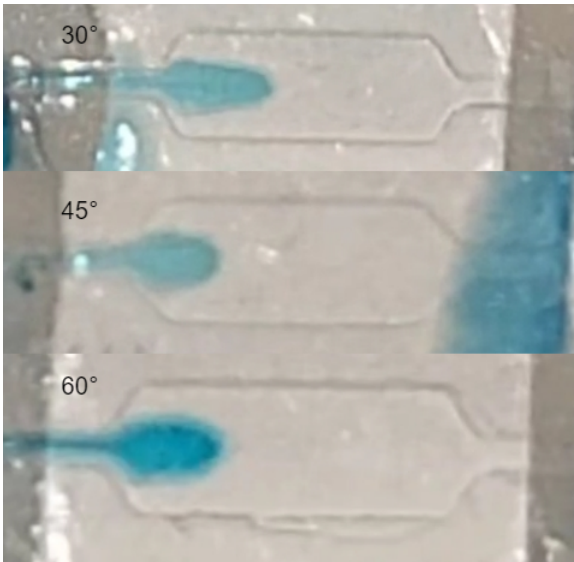
FIGURE 9. Experimental results of a 200μm height chip at 30, 45, and 60 degree inlet angles.

grees were explored. The simulation results are displayed using contour plots in Figure 11. In the figure, the channels are stacked from top to bottom with inlet angles of 30, 45, and 60 respectively. Inspection of Figure 11 indicates that the CFD model predicts a perfectly symmetric, single viscous finger for each channel. This indicates that the instability was not obtained for the flow conditions modeled. This single viscous finger looks thinner in the channel with the 30 degree inlet angle and rounder in


FIGURE 10. Experimental results of a 60μm height chip at 30, 45, and 60 degree inlet angles.

the channel with the 60 degree inlet angle. Note that the incoming flow has detached in all cases, hence, this appears to be a result of the increased volume to diffuse into.

In addition, Figure 12 also shows that the volume of fluid at t = 0.3s reaches different lengths for each channel angle. This is because for smaller inlet angles the channel area is decreased, accelerating the speed at which the low viscous fluid travels through the channel. This difference in velocity for the volume of fluid of ethanol can clearly be seen at a later time stamp of 1 second in Figure 13. The contour plots also show that the channel with the smaller inlet angle is able to generate a larger viscous finger faster and complete its way through the entire device than the channel with the larger inlet angle.

These results are expected as the larger channels generate a larger interface between the two liquids. A large interface creates more resistance for the incoming liquid. This higher resistance in turn decelerates the incoming liquid speed as it travels through the channel. The angle size increments were 15 degrees between each channel, however the jump in isosurface size between channels 1 and 2 is larger than the jump between channels 2 and 3. Another observation from the plot in Figure 13 is that the channel with larger inlet angles is able to produce slightly larger viscous fingers (isosurface increase versus 15 degree channel increase). This can be explained by the larger inlet angles generating larger channel chambers. The larger chambers in turn, allow the less viscous liquid to spread more and create a bigger viscous finger. Complimentary to the inlet and outlet angle, the channel height will have an effect on the finger velocity and propagation rate [6], but whether the inlet angles or the channel height have bigger effect on the finger propagation has yet to be explored. In addition the CFD result shows similar behavior to the physical validation experiment. The CFD simulation is well able to replicate the shape of the viscous finger shape and the number of
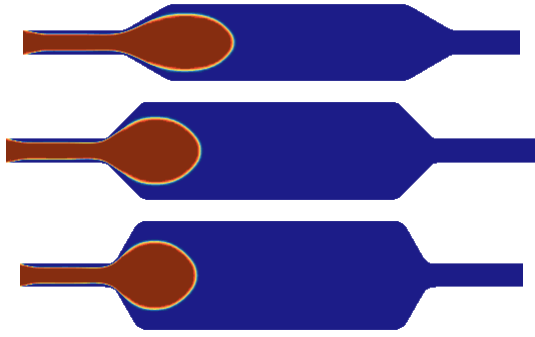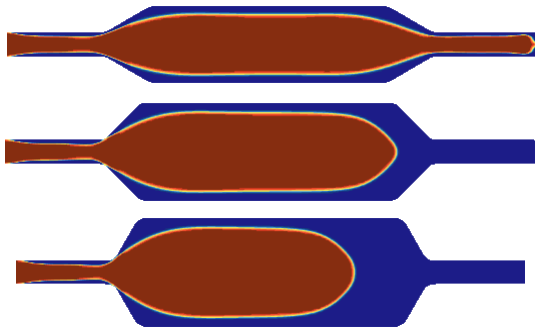
FIGURE 11. Viscous finger at 0.3s for varying channel inlet angles.
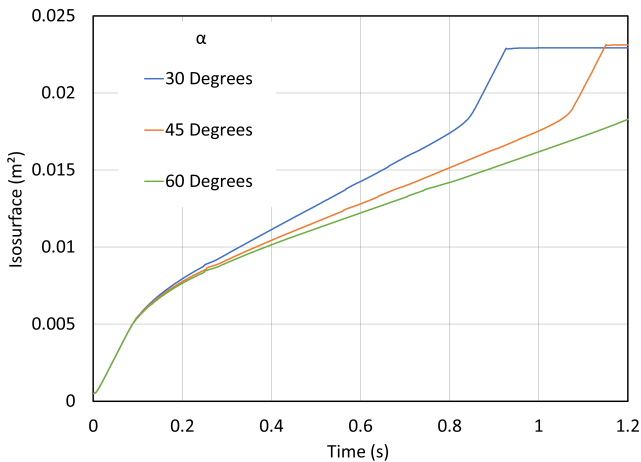
FIGURE 12. Estimated interfacial surface area for different inlet angles (α) vs. time.

FIGURE 13. Viscous finger at 1s for varying channel inlet angles.

fingers present in the channel.

The experimental results show to be similar to the CFD predictions. The images of these results were taken around the same time as the CFD simulations (t=0.3s), to the best of our abilities. In the 700μm channel height, shown in Figure 8, we can see the shape of the viscous finger as the ethanol (blue) enters into the corn syrup filled channels. The 30 degree channel has a viscous finger longer than the 45 and 60 degree channels, which was predicted by the CFD software.

Figure 9 shows the experimental results from the 200μm channel height, but has significant differences from the CFD. All three of the channels with varying inlets show a viscous finger that is much longer compared to its width. This could be due to improper set up, such as bubbles in the inlet of the microfluidic device. Even so, the instabilities still show a pattern of being farther along in the 30 degree channel compared to the 60 degree channel.

Figure 10 shows the results from the 45 and 60 degree inlet and outlet devices. Due to experimental testing issues, the 30 degree device will not be included in this study. The 45 and 60 degree viscous fingers are similar to the CFD prediction. However, the 45 degree channel appears smaller than the 60 degree. This could be due to improper experiment setup, or incorrect timing when capturing data.

Overall, the CFD simulations and experimental results showed similar results, therefore giving confidence in the CFD results. More in lab experiments can be done to further verify the outcome, due to bubbles and leaks during the experiments.

Conclusion

Different channel inlet angles were tested to see their effect on viscous finger formation. The experiment was first simulated using the CFD software Star-CCM+ and then validated by replicating the study experimentally. This was done by pre-filling a microfluidic device channel with a high viscous fluid and injected with a low viscous fluid at the inlet at a velocity. The results show that bigger inlet angles create viscous fingers at a slower rate than smaller inlet angles. This difference can be attributed to the higher interfacial resistance generated by the larger channels with bigger inlet angles. The result can help when designing fluid instability experiments inside microfluidic channels. The study helps to optimize the channel inlet and outlet angles to understand primary viscous finger formation. The results also help predict how fast the viscous finger forms and how large the viscous finger grows. The CFD simulations were experimentally replicated by creating microfluidic devices with inlet and outlet angles of 60, 45, and 30 degrees and using the same liquids. The accuracy of the CFD results, when compared to the validation testing, indicates that CFD can help in future microfluidic experiments when testing for fluid instabilities using different geometries. Future work may include a higher quality camera for higher resolution experimental data. Another improvement would be to recreate the devices, with the same varying inlet and outlet angles, while fixing the cross-sectional area (channel width). This would answer the question of which parameter is a more important factor in the rate at which viscous fingers appear; inlet and

outlet angles or cross-sectional area.

REFERENCES

[1] Nijhuis, J., Schmidt, S., Tran, N. N., and Hessel, V., 2022. "Microfluidics and Macrofluidics in Space: ISS-Proven Fluidic Transport and Handling Concepts". *Frontiers in Space Technologies, 2*, 1.

[2] Canfield, P. J., Bronowicki, P. M., Chen, Y., Kiewidt, L., Grah, A., Klatte, J., Jenson, R., Blackmore, W., Weislogel, M. M., and Dreyer, M. E., 2013. "The capillary channel flow experiments on the International Space Station: Experiment set-up and first results". *Experiments in Fluids, 54*(5), 5.

[3] Dunbar, B., 2012. Preventing bone loss in space flight with prophylactic use of bisphosphonate: Health promotion of the elderly by space medicine technologies. Last accessed 16 May 2022.

[4] McCarthy, I. D., 2005. "Fluid shifts due to microgravity and their effects on bone: A review of current knowledge". In Annals of Biomedical Engineering, Vol. 33, pp. 95–103.

[5] Smirnov, N., Dushin, V., Nikitin, V., Ivashnyov, O., Logvinov, O., Thiercelin, M., and Legros, J., 2006. "Viscous fluids flow in porous media.". In 57th International Astronautical Congress, American Institute of Aeronautics and Astronautics.

[6] P. G. Saffman, and Sir Geoffrey Taylor, F., 1958. "The penetration of a fluid into a porous medium or Hele-Shaw cell containing a more viscous liquid".

[7] Pauwelyn, T., Stahl, R., Mayo, L., Zheng, X., Lambrechts, A., Janssens, S., Lagae, L., Reumers, V., and Braeken, D., 2018. "Reflective lens-free imaging on high-density silicon microelectrode arrays for monitoring and evaluation of in vitro cardiac contractility". *Biomedical Optics Express, 9*(4), 4, p. 1827.

[8] Stahl, R., Vanmeerbeeck, G., Lafruit, G., Huys, R., Reumers, V., Lambrechts, A., Liao, C.-K., Hsiao, C.-C., Yashiro, M., Takemoto, M., Nagata, T., Gomi, S., Hatabayashi, K., Oshima, Y., Ozaki, S., Nishishita, N., and Kawamata, S., 2014. "Lens-free digital in-line holographic imaging for wide field-of-view, high-resolution and real-time monitoring of complex microscopic objects". In Imaging, Manipulation, and Analysis of Biomolecules, Cells, and Tissues XII, Vol. 8947, SPIE, p. 89471F.

[9] Shokri, H., Kayhani, M. H., and Norouzi, M., 2018. "Saffman–Taylor instability of viscoelastic fluids in anisotropic porous media". *International Journal of Mechanical Sciences, 135*, 1, pp. 1–13.

[10] Zimmerman, W. B., and Homsy, G. M., 1992. "Three-dimensional viscous fingering: A numerical study". *Physics of Fluids A: Fluid Dynamics, 4*(9), 9, pp. 1901–1914.

[11] Chandorkar, A., and Palit, S. Simulation of Droplet-based Microfluidics Devices using a Volume of Fluid (VOF) Approach. Tech. rep.

[12] Renardy, M., Renardy, Y., and Li, J., 2001. "Numerical Simulation of Moving Contact Line Problems Using a Volume-of-Fluid Method". *Journal of Computational Physics, 171*(1), 7, pp. 243–263.

[13] Siemens, 2020. StarCCM+ V15.02.009 Usersguide.